International Journal of Heat and Mass Transfer 235 (2024) 126153

Contents lists available at ScienceDirect

International Journal of Heat and Mass Transfer

journal homepage: www.elsevier.com/locate/ijhmt

Refinement of the thermo-osmotic velocity calculation methodology and investigation of control strategies

Wenhao Fan, Ji Li, Yubo Tan, Yifan Zhang, Wei Liu, Zhichun Liu *

School of Energy and Power Engineering, Huazhong University of Science and Technology, Wuhan 430074, China

ARTICLE INFO

Keywords:
Thermo-osmosis
Viscosity
Excess specific enthalpy
Nanoconfined fluid
Molecular dynamics simulation

ABSTRACT

Thermo-osmosis holds broad application prospects in low-grade heat energy utilization, seawater desalination, and biomedicine. However, fluid near-wall adhesion and changes in physical properties are ignored in calculating thermo-osmotic velocity, which obscures the mechanism of thermo-osmosis. To address this issue, we refine the thermo-osmotic velocity formula by incorporating the spatial variation of viscosity. Additionally, the near-wall adhesion and the density stratification properties of the fluid are analyzed to determine the effective region of thermo-osmosis, thereby facilitating the quantitative calculation of the local velocity. Furthermore, the accuracy of the calculations is validated via molecular dynamics simulations. Under the given boundary conditions within the slit, taking the direction of increasing temperature as the positive direction, the average thermo-osmotic velocities obtained from simulation and refined calculation method are -0.113 m/s and -0.105 m/s, respectively. The correlation coefficient of the velocity distribution, derived through multiple simulations and calculations, is approximately 0.63, while the error in the thermo-osmotic flux is about 7.0 %. Conversely, if viscosity variations are ignored under the same conditions, the calculated average thermo-osmotic velocity is 0.036 m/s, which significantly differs from the simulation value in both magnitude and direction. Subsequently, the impacts of various influential factors are systematically analyzed to elucidate control methods for thermo-osmosis. The findings indicate that system temperature, pore size, and membrane hydrophilicity significantly influence thermo-osmosis by altering the liquid's viscosity and excess specific enthalpy. Conversely, the geometry of the membrane pores has a relatively minor effect. Moreover, utilizing the refined calculation method, we elucidated the roles of the aforementioned factors in both flow resistance and generalized driving forces, thereby delineating their impacts on thermo-osmosis. Overall, this study elucidates the mechanism of thermo-osmosis and identifies effective control methods, offering suggestions for the practical application of thermo-osmosis.

1. Introduction

Since its initial identification in the early 20th century, thermo-osmosis has garnered considerable attention from researchers [1,2]. The ability of thermo-osmosis to facilitate directional fluid transport at interfaces with temperature gradients [3,4] heralds significant potential in utilizing clean and renewable energy sources [5,6], improving energy efficiency [7], and developing micro/nano-motors [8]. Against the backdrop of increasing energy shortages, the vast majority of low-grade thermal energy (< 100°C), represented by geothermal energy and industrial waste heat, has not been effectively utilized [9,10]. It is reported that more than 30 % of global primary energy consumption is dissipated in the form of low-grade heat [11]. Effective recycling of low-grade thermal energy can not only alleviate the energy crisis and optimize the energy structure, but also effectively reduce carbon emissions and mitigate the greenhouse effect [12,13]. Utilizing thermo-osmotic energy conversion (TOEC) technologies enables the directional migration of fluid against the pressure gradient to store potential energy under a relatively low temperature heat source (< 100 °C), thereby facilitating the recapture of low-grade heat energy with substantial application potential [14,15].

Despite the significant potential for thermal osmosis, its performance in many applications often falls short of expectations. For instance, in the TOEC system, thermal osmosis converts low-grade heat into potential energy. Our preliminary simulations also indicate that thermal osmosis can drive fluid flow against the pressure gradient, as illustrated in Fig. A1 of Appendix A. However, in practical applications, the energy conversion efficiency of thermal osmosis is typically quite low; even in laboratory settings, the single-stage thermal osmosis energy conversion

* Corresponding author.
E-mail address: zcliu@hust.edu.cn (Z. Liu).

https://doi.org/10.1016/j.ijheatmasstransfer.2024.126153
Received 11 June 2024; Received in revised form 14 August 2024; Accepted 31 August 2024
Available online 7 September 2024

Nomenclature

B	slit width (m)
b	slip length (m)
d	dimensionality of the system
f_i	interparticle force (N)
f_x	external force applied per unit volume of fluid (N/m^3)
H_0	enthalpy per unit volume of the bulk liquid (J/m^3)
h	half of the slit height (m)
h_s	thickness of the boundary layer with significant enthalpy change (Å)
δH	enthalpy change per unit volume of the bulk liquid resulting from membrane interactions (J/m^3)
J	heat transfer rate (J/s)
k_B	Boltzmann constant (J/K)
l	membrane thickness, which is the length of the slit channel (m)
ΔP	pressure difference (Pa)
Q	volume flux (m^3/s)
r_i	particle spacing (m)
T	average temperature of the system (K)
ΔT	temperature difference between the two sides of the membrane (K)
∇T	temperature gradient (K/m)
v	liquid transmembrane velocity (m/s)
v_s	slip velocity (m/s)

Greek symbols

β_{ij}	phenomenological coefficients
ε	energy parameters of L-J potential (J)
ξ	hydrophilicity coefficient
η	viscosity (Pa·s)
λ	friction coefficient (Pa·s/m)
μ	Gibbs free energy per unit volume of the bulk liquid (J/m^3)
ρ	density (kg/m^3)
σ	distance parameters of L-J potential (m)

Abbreviations

EAM	embedded atom method
EMD	equilibrium molecular dynamics
ESE	enthalpy change per unit volume of the bulk liquid resulting from membrane interactions (J/m^3)
IED	internal energy density (Pa)
LAMMPS	Large-scale Atomic/Molecular Massively Parallel Simulator
L-J	Lennard-Jones
MD	molecular dynamics
NVE	microcanonical ensemble
PDF	pressure-driven flux (mol/(m^2·s))
PEM	proton exchange membrane
PEMFC	proton exchange membrane fuel cell
TOEC	thermal osmotic energy conversion
TOF	thermo-osmotic flux (mol/(m^2·s))

Subscripts

ave	average value of the physical properties
P	pressure-driven
S-L	between solid and liquid particles
x	in the X-axis direction
α, β	one of the x, y, and z directions

efficiency often falls below one-tenth of the theoretical efficiency [5,6]. Many researchers resort to altering external conditions to enhance the efficiency, such as applying negative pressure [5] or employing multi-stage stacking [6], to enhance the utilization efficiency of thermal energy. In proton exchange membrane fuel cells (PEMFCs) [16,17], although thermal osmosis plays a role in the transport of hydrated protons [18], current research suggests that thermal osmotic forces have a detrimental effect [19], but there is no ongoing research aimed at mitigating this adverse effect. In summary, the shortcomings in these applications primarily stem from inadequate research on thermal osmosis, with its influencing mechanisms remaining unclear. Consequently, it is challenging to discern patterns and develop optimization criteria.

Thermal osmosis is the phenomenon of liquid directional flow induced by a temperature gradient at the fluid-solid interface [20,21]. The applications of thermal osmosis are often linked to porous membranes due to their high surface area-to-volume ratio and ultrathin thickness, which ensure sufficient fluid-solid contact surface and temperature gradient. When there is a temperature difference between the two sides of a membrane, the temperature gradient within its porous structure promotes the transmembrane transport of liquid. Based on whether the transmembrane fluid is in a liquid state, thermal osmosis can be categorized into liquid-gap thermal osmosis and gas-gap thermal osmosis. Gas-gap thermo-osmosis is driven by the evaporation and condensation of the liquid at both ends of the pore, with the fluid always moving from the hotter to the cooler end under the same external pressure. The driving mechanism of liquid-gap thermo-osmosis is more complex and is generally considered to be governed by solid-liquid particle interactions near the solid-liquid interface under temperature gradients. The flow direction and magnitude are affected by numerous factors [22,23]. Due to liquid-gap thermo-osmosis occurring at the nanometer scale, most experimental apparatuses are only able to determine the size and direction of the thermo-osmotic flux (TOF), but cannot measure the local physical properties at this scale. This limitation makes the thorough analysis of the nanoscale mechanism of liquid-gap thermo-osmosis challenging. Therefore, researchers have predominantly investigated the mechanism of liquid-gap thermo-osmosis through theoretical derivation and simulation verification [24]. This paper primarily focuses on liquid-gap thermo-osmosis. Unless otherwise stated, all subsequent mentions of thermo-osmosis refer to its liquid-gap type.

At present, the method for calculating the liquid-gap thermo-osmotic velocity that is widely acknowledged and employed by the scientific community is the formula derived by Derjaguin [22,25], which is based upon Onsager reciprocity relations [26]. However, this calculation method still requires significant improvement for enhanced accuracy. Recently, Ganti et al. [22] presented three methods for calculating thermo-osmotic velocity, which all produced similar results. They calculated a Soret coefficient $S_T \sim 0.047$ K^{-1}, which is of the order of magnitude of 0.014 K^{-1} in the research [27]. It reveals that the current thermo-osmotic velocity calculation is complex and can be more accurate. Therefore, in the research outlook Ganti suggested that incorporating viscosity changes could refine the equation for thermo-osmotic velocity. Anzini et al. [28] extended the linear response theory to heterogeneous systems to obtain an accurate nanoscale theory of thermo-osmosis. They showed that the calculation of thermo-osmotic velocity is constrained by size. In experimental studies, it is also reviewed that many experiments measured the direction of thermo-osmosis even opposite to the theory [1]. It follows that there remains a necessity for a more refined theoretical framework for liquid-gap thermo-osmosis.

As previously mentioned, thermo-osmosis plays a significant role in numerous applications, such as TOEC systems and PEMFCs. Furthermore, in recent years, researchers have also been investigating its

application in membrane-venting heat sinks [29]. However, without a thorough understanding of the mechanisms influencing thermo-osmosis, researchers cannot optimize its potential benefits in these applications. Refinement of the mechanistic study is imperative to establish optimization criteria and provide a basis for regulation in thermo-osmotic applications [19,30]. However, current research has yet to effectively refine traditional computational methods, lacking a theoretical approach that closely aligns with microscopic simulation results. Hence, this study will refine the existing method for calculating thermo-osmotic velocity and validate the revised theory by analyzing various factors influencing thermo-osmosis. Additionally, this analysis also conducts a feasibility assessment for formulating optimization criteria for thermo-osmosis in diverse applications.

The innovations presented in this paper primarily encompass the following: (1) Firstly, the formulation for calculating thermo-osmotic velocity has been revised to account for variations in viscosity; (2) Secondly, the effective flow region for thermo-osmosis has been delineated based on fluid near-wall adhesion and density stratification; (3) Thirdly, employing the enhanced calculation formula and the identified effective flow region, we quantitatively obtained the distribution of thermo-osmotic velocity, which exhibited a remarkably small error when compared to molecular dynamics (MD) simulation results, with the thermo-osmotic flux error amounting to merely 7.0 %; (4) Fourthly, we analyzed the impacts of four factors on thermo-osmosis and elucidated the underlying mechanisms using the refined theory.

Our research focuses on the mechanistic analysis of thermo-osmosis and the exploration of control methods. In Section 2, the variation in fluid viscosity is considered, and a refined quantitative calculation formula for the distribution of thermal osmosis velocity is derived. In Section 3.2, we analyze the properties of the thermo-osmotic fluid and delineate the effective flow region, in which the thermo-osmotic velocity distribution is calculated and the accuracy of the theoretical calculations are validated by MD simulations. In order to determine the effective regulation mechanism, the effects of various factors on the thermo-osmosis are investigated by MD simulation in Section 3.3. It is worth noting that membrane hydrophilicity has a strong influence on thermo-osmosis; a change in hydrophilicity not only significantly alters the magnitude of the thermo-osmotic flux (by 3-10 times), but also changes the direction of flow. The above studies have explored the mechanism of thermo-osmosis, determined effective regulation criteria, and offered insights for thermo-osmosis to fulfill a beneficial role in practical applications.

2. Mechanism and formula derivation

Based on the Gibbs-Duhem equation, and Onsager reciprocity relations, the relationship between thermo-osmotic velocity and excess specific enthalpy (ESE), liquid viscosity, and temperature gradient can be deduced. First, based on irreversible thermodynamics, the coupled liquid flow and heat transfer equations can be expressed by the following two expressions respectively [31,32]:

$$Q = -\beta_{11}\Delta P - \beta_{12}\frac{\Delta T}{T} \tag{1}$$

$$J = -\beta_{21}\Delta P - \beta_{22}\frac{\Delta T}{T} \tag{2}$$

where Q is the volume flux (in m^3/s) and J is the heat transfer rate (in J/s) [25], β_{ij} is the phenomenological coefficients (β_{11} refers to the coefficient of pressure difference on volume flux, in $m^3/(s{\cdot}Pa)$, β_{12} refers to the coefficient of temperature difference on volume flux, i.e., the thermo-osmotic coefficient, in m^3/s), ΔP is the pressure difference, T is the average temperature of the system, and ΔT is the temperature difference between the two sides of the membrane. According to Onsager reciprocity relations, $\beta_{12} = \beta_{21}$, which has been proved by the researchers using MD simulation [26].

Taking the slit model studied in this paper as an example, as shown in Fig. 1 (a), we assume that all pores are plane-parallel slits, which is consistent with Derjaguin's research model. The membrane thickness is denoted by l, oriented along the x-axis; the slit width is represented by B, aligned with the y-axis; and the slit height is characterized by $2h$, directed along the Z-axis. Two horizontal solid walls are configured parallel to the x-y plane, with liquid molecules occupying the slit space between them.

To determine β_{12}, it is imperative to first compute β_{21}. Consider a pressure-driven transmembrane liquid flow with an isothermal heat flux of:

$$J_P = \mathrm{H}_0 Q_P + B\int_0^{2\mathrm{h}} \delta H(\mathrm{z}) v_P(\mathrm{z}) d\mathrm{z} \tag{3}$$

where, H_0 represents the enthalpy per unit volume of the bulk liquid, in J/m^3, δH signifies the enthalpy change per unit volume of the bulk liquid resulting from membrane interactions, which we define as the ESE, in J/m^3, v indicates the liquid transmembrane velocity, in m/s, and the subscript P indicates that the flow is pressure-driven. z = 0 or z = $2h$ means on one side of the flow channel. The liquid's enthalpy was derived from the MD simulation software by summing the total energy of each atom and the product of pressure and volume, with both the total energy and pressure being calculated from the relative positions of the particles according to the potential function. Clearly, in the absence of the membrane, the heat transfer flux would be (H_0Q_P) for the same flux. Therefore, the presence of the membrane influences the heat transfer flux as follows:

$$J = B\int_0^{2\mathrm{h}} \delta H(\mathrm{z}) v_P(\mathrm{z}) d\mathrm{z} \tag{4}$$

Derjaguin's study [25] assumed the viscosity η to be constant and obtained a parabolic velocity profile described by Poiseuille's law:

$$v_P(z) = -\frac{(2hz - z^2)}{\eta}\frac{\Delta P}{l} \tag{5}$$

Substituting Eq. (5) into Eq. (4) yields:

$$J = -\frac{B\Delta P}{\eta l}\int_0^{2\mathrm{h}} \delta H(\mathrm{z})\left(2hz - z^2\right) d\mathrm{z} \tag{6}$$

According to Onsager reciprocity relations [26], the thermo-osmotic coefficient β_{12} can be expressed as:

$$\beta_{12} = \beta_{21} = -\frac{B}{\eta l}\int_0^{2\mathrm{h}} \delta H(\mathrm{z})\left(2hz - z^2\right) d\mathrm{z} \tag{7}$$

Derjaguin [25] assumes that the enthalpy of the liquid changes only in a thin boundary layer h_s near the wall, which is much smaller than h. Then the velocity profile can be assumed linear at z < h_s: $v(z) = -2hz\Delta P/(\eta l)$. Substituting the above assumptions into Eq. (7) gives:

$$\beta_{12} = \beta_{21} = -\frac{4Bh}{\eta l}\int_0^{h_s} \delta H(\mathrm{z}) z d\mathrm{z} \tag{8}$$

Given the parameter β_{12}, the average liquid velocity v_x traversing the membrane exclusively driven by the temperature difference of ΔT can be expressed as

$$v_x = -\frac{2}{\eta l}\int_0^{h_s} \Delta H(\mathrm{z}) z \frac{\Delta T}{T} d\mathrm{z} = -\frac{2}{\eta}\int_0^{h_s} \delta H(\mathrm{z}) z \frac{\nabla T}{T} d\mathrm{z} \tag{9}$$

where $\nabla T = \Delta T/l$, represents the temperature gradient in the direction of the flow channel, i.e., the x-axis direction.

The analysis indicates that the aforementioned approach provides an approximate estimation of the average velocity of thermo-osmotic flow; however, certain assumptions underlying this method are not sufficiently justified. Firstly, liquid-gap thermo-osmosis occurs in membranes featuring nanoscale pore dimensions, where the liquid is

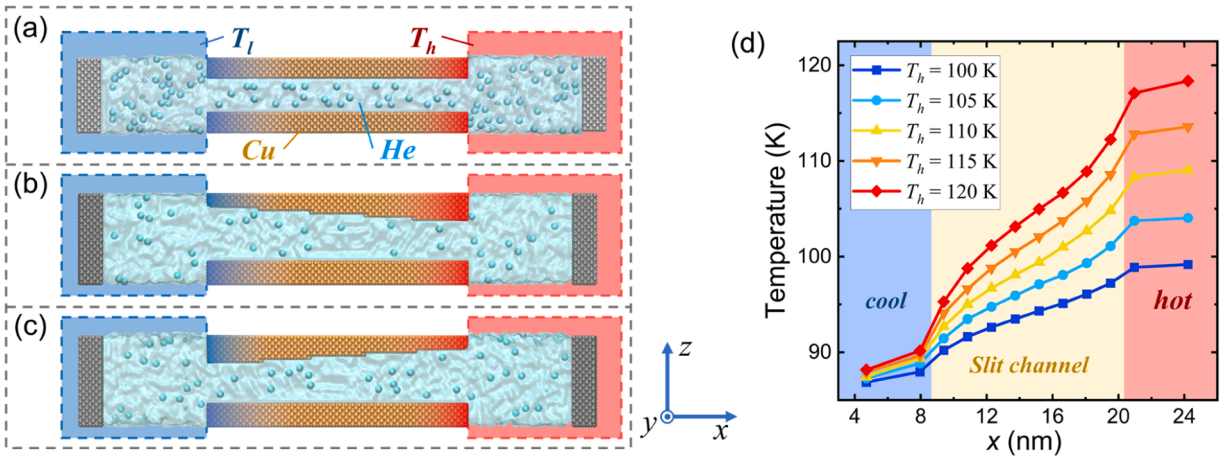

Fig. 1. Thermo-osmotic model and liquid temperature distribution: (a) Equal-height slit model; (b ~ c) Non-equal-height slit model; (d) Liquid temperature distribution on the channel axis (x-axis) for different hot end temperature (T_h) conditions.

confined to the nanoscale in at least one dimension, a state referred to as nanoconfined liquid. A notable characteristic of nanoconfined liquid is the significant alteration in its physical properties relative to those of the bulk liquid, including viscosity, enthalpy, and others. Furthermore, these changes are inhomogeneous, with the varying distance from the wall substantially influencing the degree of alteration in physical properties. Consequently, the variation in viscosity must be taken into account when determining the distribution of pressure-driven flow. Secondly, for the pressure-driven flow, despite the high ESE near the wall (as will be verified by the MD simulation presented later), the flow rate in this region is comparatively lower than that at the center of the flow channel. Conversely, while the ESE of the liquid at the center of the channel is relatively low, the high flow rate in this area renders its contribution to heat flow significant. Consequently, the derivation from Eq. (7) to Eq. (8) presents certain issues.

To solve the above problem, Cecilia et al. [33] simplified the Navier-Stokes equations based on the thermo-osmosis model:

$$-\eta\frac{\partial^2 v_x}{\partial z^2} = -\frac{\partial P}{\partial x} + f_x \tag{10}$$

where f_x is the external force applied per unit volume of fluid, i.e., the force density (in N/m^3).

The integration of Eq. (10) is performed when the pressure gradient in the x-direction is zero. Given the symmetry of the velocity within the flow channel about its central axis, the following result is derived:

$$\left.\frac{\partial v_x}{\partial z}\right|_{z=h} = 0 \tag{11}$$

$$\frac{\partial v_x}{\partial z}(\mathrm{z}) = -\int_h^z \frac{1}{\eta} f_x(z')dz' = \int_z^h \frac{1}{\eta} f_x(z')dz' \tag{12}$$

The integration of Eq. (12) is continued over the range from 0 to z:

$$v_x(z) - v_x(0) = \int_0^z dz' \int_{z'}^h \frac{1}{\eta} f_x(z'')dz'' \tag{13}$$

Considering the Navier boundary conditions [34]:

$$v_s = b\left.\frac{\partial v_x}{\partial z}\right|_{z=0} \tag{14}$$

where v_s is the interfacial velocity jump of the fluid at the wall, also known as slip velocity. λ is the friction coefficient, and $b = \eta/\lambda$ is the slip length, which depends on the interaction between solid-liquid particles. And for hydrophilic walls b is generally taken to be zero [35].

Substituting Eq. (14) into Eq. (13) yields:

$$v_x(z) = \int_0^z dz' \int_{z'}^h \frac{1}{\eta} f_x(z'')dz'' + b\int_0^h \frac{1}{\eta} f_x(z)dz \tag{15}$$

In the study of thermo-osmosis, the force density driving the flow will be the thermodynamic force [33]:

$$f_x = -T\frac{d(\mu/T)}{dx} \tag{16}$$

where μ is the Gibbs free energy. Taking into account the Gibbs-Helmholtz equation:

$$\frac{d(\mu/T)}{dT} = -\frac{\delta H}{T^2} \tag{17}$$

where δH represents the ESE mentioned earlier. Substituting Eq. (17) into Eq. (16) yields the expression for f_x:

$$f_x(z) = -\delta H(z)\frac{\nabla T}{T} \tag{18}$$

Substituting Eq. (18) into Eq. (15) yields the calculated equation for the thermo-osmotic velocity distribution:

$$v_x(z) = -\frac{\nabla T}{T}\left\{\int_0^z dz' \int_{z'}^h \frac{1}{\eta}\delta H(z'')dz'' + b\int_0^h \frac{1}{\eta}\delta H(z)dz\right\} \tag{19}$$

Equation (19) connects the thermo-osmotic velocity v_x with liquid viscosity η, the ESE δH, and temperature gradient ∇T. Analysis reveals that, the thermo-osmotic velocity points to the direction of temperature reduction when δH is greater than zero. Conversely, when δH is less than zero, the thermo-osmotic velocity points to the direction of increasing temperature. A reduction in liquid viscosity, an augmentation in the absolute value of the ESE, or an enhanced temperature gradient contributes to an increase in thermo-osmotic velocity and vice versa.

Upon comparing Eq. (9) and Eq. (19), it becomes apparent that the former only considers the variations in fluid properties near the wall, thus allowing only for the calculation of the average thermo-osmotic velocity within the flow channel. Meanwhile, the latter incorporates all localized fluid properties in the flow channel into the velocity calculation and is capable of accurately determining the thermo-osmotic velocity at each localized position, thus offering a more precise and rigorous approach.

3. Molecular dynamics simulations and results

In this research, MD simulation method is employed to explore the nanoscale mechanisms of thermo-osmosis, as it enables concurrent nanoscale flow simulation, local particle energy visualization, and local

physical property calculation. We will conduct MD simulations to investigate the thermo-osmosis behavior of liquid argon confined within a copper nano-slit. Given that argon is a monatomic molecule with highly stable chemical properties and electrical neutrality, the interactions between argon atoms and other microscopic particles are relatively simple. Selecting argon as the simulation medium offers several advantages: (1) In molecular dynamics simulations, argon atoms are only influenced by the Lennard-Jones potential, which conserves computational resources and accelerates the calculation process; (2) As this study primarily aims to explore the underlying mechanisms of thermo-osmosis, choosing a medium with simple mechanical properties helps eliminate interference from other factors, ensuring that the research findings are solely attributable to the effects of thermo-osmosis. Employing water or other media would complicate the analysis by introducing influences from hydrogen bonds, electric dipole moments, and charge distributions, which are disadvantageous for mechanistic research. Consequently, despite its inapplicability as a thermo-osmosis workpiece in practical applications, argon is highly suitable for in-depth analysis of the mechanism underlying the phenomenon. The use of a slit structure as the flow channel enhances the statistical analysis of local physical properties and aligns with the practical applications of membrane slit channels. The Lennard-Jones (L-J) potential and the embedded atom method (EAM) potential are selected for the simulation, with the specifics of inter-particle potential functions and their parameters detailed in Table 1.

Based on the slit model, MD simulations will be conducted to prove the correctness of the theoretical calculations in Chapter 2, followed by elucidating the effects of four critical factors on thermo-osmosis: system temperature, pore size, pore geometry, and the hydrophilicity of nanoporous membranes.

3.1. Model description

To elucidate the impacts of system temperature, pore size, pore geometry, and membrane hydrophilicity on thermo-osmosis, this study conducted simulations by systematically varying the hotter end temperature, slit height, channel geometry, and channel wall hydrophilicity.

The thermo-osmotic model, depicted in Fig. 1 (a), with a liquid storage zone on both sides. These reservoirs are exposed to a piston pressure of 1.0 bar, and the copper nano-slit fixed in the middle acts as a porous medium with a slit channel length of 14.5 nm. To investigate the pore geometry's effect on TOF, the slit was modified to have unequal heights, as illustrated in Fig. 1 (b) and Fig. 1 (c). Periodic boundary conditions are applied in the y and z directions to mitigate the influence of size effects, while the x direction employs a shrink-wrapping boundary condition that dynamically adjusts to the piston's movements. All simulations utilize the NVE ensemble, which ensures that the number of atoms in the system (N), the total volume of the system (V), and the total energy of the system (E), remain constant. And the liquid's temperature distribution being indirectly regulated by the Langevin thermostat. This thermostat controls the temperature of selected Cu atoms at both ends of the porous medium, thus minimizing direct interference with the liquid particles' motion and enhancing the simulations' validity.

In all simulations, copper atoms at the system's cold end are maintained at 86 K, while those at the hotter end are kept at 110 K. When investigating the impact of system temperature on thermo-osmosis, the hot end temperatures (T_h) are set at 100, 105, 110, 115, and 120 K for different trials. The temperatures of the hot and cold ends are set in this manner because, at a pressure of 1 bar, argon has a very low boiling point. This study ensures the internal pressure is maintained at 1 bar by applying an external force through pistons on both sides. Additionally, at the nanoscale, the intermolecular forces significantly impact the behavior of fluid particles. Thus, within the confined nanoscale space of this model, argon remains in a liquid state within the specified temperature range of the hot and cold ends. Moreover, the resulting temperature gradient in the channel is substantial, allowing the simulation to observe a pronounced thermo-osmosis flow within a relatively short period, thereby conserving computational resources.

Table 1
Potential type and parameter [36]

Atom	Potential type	ε (eV)	σ (Å)
Ar- Ar	L-J	0.0104	3.405
Ar-Cu	L-J	0.0653	2.8725
Cu- Cu	EAM		

Upon reaching stabilization, the system operates freely for 100 ns under a temperature gradient after which the TOF is quantified for each simulation. TOF is quantified as the molar number of liquid particles traversing the established temperature gradient, per unit time and per unit area of the flow channel cross-section. Fig. 1 (d) displays the temperature distribution profiles within the liquid for systems subject to varying hot end temperatures. The data illustrate that reservoir temperatures closely align with the predefined values, and the temperature gradient within the nano-channel is relatively uniform, indicating a stable temperature gradient along the channel's axis (x-axis).

The model's slit height ($2h$) was set at 2.89 nm, and additional MD models featuring slit heights of 2.17, 2.53, 2.89, 3.25, and 3.61 nm were constructed to examine the influence of pore size on thermo-osmosis. It is important to note that the slit heights denote the spacing between particles on the upper and lower wall surfaces. Due to the spacing maintained by particle interactions, the actual range of free movement for liquid particles is somewhat diminished relative to the slit heights [37,38]. To assess pore geometry's impact on thermo-osmosis, the liquid flow channel is modeled as a slit with varying heights, 3.25 nm on the wider side and 2.53 nm on the narrower, as depicted in Fig. 1 (b) and Fig. 1 (c). The model employed in this study is comparable in size to those of other existing studies [24,39], allowing for simulations that are neither excessively lengthy nor devoid of significant observations.

This study employs the hydrophilicity coefficient ξ to denote the membrane's hydrophilicity level, defined as the ratio of solid-liquid particle potential energy intensity to that of liquid-liquid particle interactions. With a hydrophilicity coefficient of 6.28 for Cu and Ar, MD simulations indicate a contact angle approaching 0°. To investigate how the hydrophilicity coefficient affects thermo-osmosis in porous membranes, 12 materials with coefficients ranging from 0.1 to 10.0 are compared, and the variations in contact angle are presented in Fig. 2.

3.2. Characterization of liquid in thermo-osmosis and validation of theoretical calculations

Prior to the analysis of simulation results and the dissection of the influence mechanisms, a comprehensive understanding of the fundamental characteristics of the liquid involved in the thermo-osmosis process is essential.

3.2.1. Density stratification of fluids

To facilitate the extraction and statistical analysis of liquid characteristics, this study establishes a slit model specific to thermo-osmosis. As detailed in Section 2, the fluid within the nano-slit is confined at the nanoscale in the slit height direction, characterized by restricted molecular motion and intense interactions with wall particles, thereby exhibiting the characteristics of nanoconfined fluid. Owing to the interaction with wall particles, the liquid's physical properties within the slit—namely, density, internal energy, and pressure—vary with the distance from the solid-liquid interface. Fig. 3 displays the density distribution curves of the liquid along the slit height for three distinct models of wall hydrophilicity coefficients, each with a slit height of 2.89 nm, demonstrating similar distribution characteristics to nanoconfined liquids [37,38]. In Fig. A2 in Appendix A, the distribution of liquid

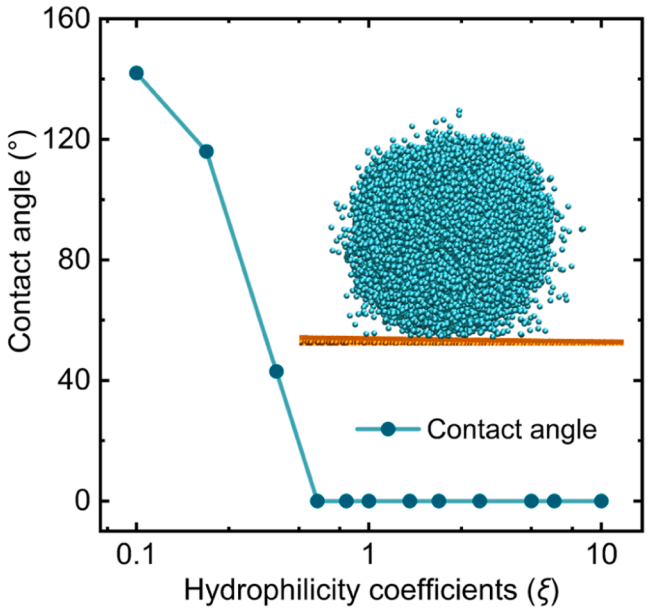

Fig. 2. Contact angles of materials with different hydrophilicity coefficients. The hydrophilicity coefficient ξ denotes the membrane's hydrophilicity level, defined as the ratio of solid-liquid particle potential energy intensity to that of liquid-liquid particle interactions.

particles within the slit is portrayed, demonstrating distinct layering characteristics.

The data presented in Fig. 3 indicate that the liquid establishes a multilayer structure with varying densities within the channel, which is similar to the results of Chen et al [24,35]. Fig. 3 (a) through Fig. 3 (d) present the simulation data from this study, demonstrating the influence of various hydrophilic materials on the fluid density within the slit. Fig. 3 (e) and (f) showcase Chen et al.'s data [35], revealing the fluid density distribution within slits of differing heights. Neighboring peaks maintain about a same distance from each other, and the peaks increase in size as they approach the wall. Even with the hydrophobic wall, possessing a hydrophilicity coefficient of 0.4, the maximum density within the adhesive layer surpasses 1.5 times the average density of the intermediate layer. The greater the hydrophilicity of the wall material, the more pronounced the impact on the water within the flow channel. A comparison of the curves in Fig. 3 reveals that the liquid density in the wall-attached layer is elevated within slits possessing higher hydrophilicity coefficients. This is attributable to a stronger adsorption of liquid particles by the wall, resulting in a greater number of particles bound to it and the presence of a several-angstroms-wide 'vacuum zone' devoid of liquid particles between the wall-attached layer and the subsequent liquid layer.

3.2.2. Near-wall adhesion of liquids

Upon comprehending the characteristics of liquid density stratification, we know that owing to the exceptionally strong interactions between solid-liquid particles, liquid particles are attracted to the solid wall to form a particle film with fairly high density. To visualize the impediment of liquid particles at varying elevational layers due to the wall, Fig. 4 illustrates the distribution of local potential energy produced by wall particles at distinct altitudes under the condition of a wall hydrophilicity coefficient of 6.28.

Three surfaces represent the distribution of local potential energy for liquid particles at varying heights resultant from their interaction with the wall particles. The distances of the liquid particles from the solid-liquid interface are 1.2 $\sigma_{S\text{-}L}$, 1.1 $\sigma_{S\text{-}L}$, and $\sigma_{S\text{-}L}$, respectively. And $\sigma_{S\text{-}L}$ represents the L-J potential distance parameter, indicating the distance at which the potential energy of interaction between solid and liquid particles is zero.. The surface contour depicted in the figure indicates that the potential energy interaction between solid and liquid particles creates 'potential wells' on the horizontal plane, influencing the movement of the liquid particles. Furthermore, the depth of the "potential well" near the wall escalates substantially, thereby augmenting the obstruction to the lateral movement of the liquid particles, confining them to a limited region.

By Fig. A1, it is noticed that the liquid particles at the walls display "quasi-lattice" properties akin to those of solids. Compared with the liquid particles in the middle of the flow channel, the liquid particles at the wall-adhesion layers are highly organized, which are almost periodically arranged in the same plane. Video V1 illustrates the dynamics of fluid particles driven by external pressure, revealing that the liquid particles within the wall-adhesion layer merely oscillate near their respective positions without undergoing flow.

To verify the correctness of the theoretical calculations, we must first remove the interference. Based on the molecular distribution, the assumption of a continuous medium holds true only for the central layers within the slit. Considering that the molecules in the wall-attached layer manifest quasi-lattice properties and are confined to vibrating at fixed sites, they must be excluded from the calculation of the thermo-osmotic velocity. The particle distribution in the "vacuum" region is almost absent, and the erratic motion of individual particles significantly influences the statistical outcomes in this region, necessitating the exclusion of particles from this region as well. Acknowledging these universal characteristics of the fluid within the pore space enhances the understanding of the thermo-osmotic mechanism and facilitates a more precise determination of the local thermo-osmotic velocity. Given the molecular distribution, the assumption of a continuous medium is applicable solely to the central layer within the slit. Our focus is exclusively on the central portion of the flow channel characterized by a continuous particle distribution when computing the thermo-osmotic velocity. Then, how to determine the velocity boundary of the fluid in the center region after excluding the liquid region near the wall becomes our concern.

3.2.3. Estimation of fluid viscosity

Considering the density stratification and near-wall adhesion of the thermo-osmosis liquid, the thermo-osmosis velocity of the liquid at different locations can be quantitatively calculated using Eq. (19). At the nanoscale, the liquid viscosity undergoes modifications due to solid-liquid interactions and small-size effects. Consequently, it is crucial to incorporate the positional variations in liquid viscosity when computing the thermo-osmotic velocity. Nonetheless, ascertaining the viscosity of the liquid at various points within the channel presents a challenge; this can be addressed through the subsequent analysis steps. Initially, per the viscosity Eq. (20), the equilibrium molecular dynamics (EMD) simulations reveal that viscosity can be statistically derived from the time autocorrelation function of the liquid pressure. Subsequently, the relationship between pressure and molar density of the fluid is elucidated by integrating Eq. (21) with the pressure data from the MD simulations in LAMMPS. Finally, the correlation between fluid viscosity and molar density can be deduced based on the established relationship between pressure and molar density.

$$\eta = \lim_{t\to\infty} \frac{V}{k_B T} \int_0^t \sum_{\alpha,\beta} \frac{1}{5} \left\langle \left\langle P_{\alpha,\beta}(t) P_{\alpha,\beta}(0) \right\rangle \right\rangle \tag{20}$$

$$P = \frac{N k_B T}{V} + \frac{1}{Vd} \sum_{i=1}^{N'} \overrightarrow{r_i} \cdot \overrightarrow{f_i} \tag{21}$$

where k_B is the Boltzmann constant, α and β represent the x, y, and z directions, $P_{\alpha,\beta}$ represent the pressure in the α-β direction, d is the dimensionality of the system, r_i is the particle spacing and f_i is the interparticle force..

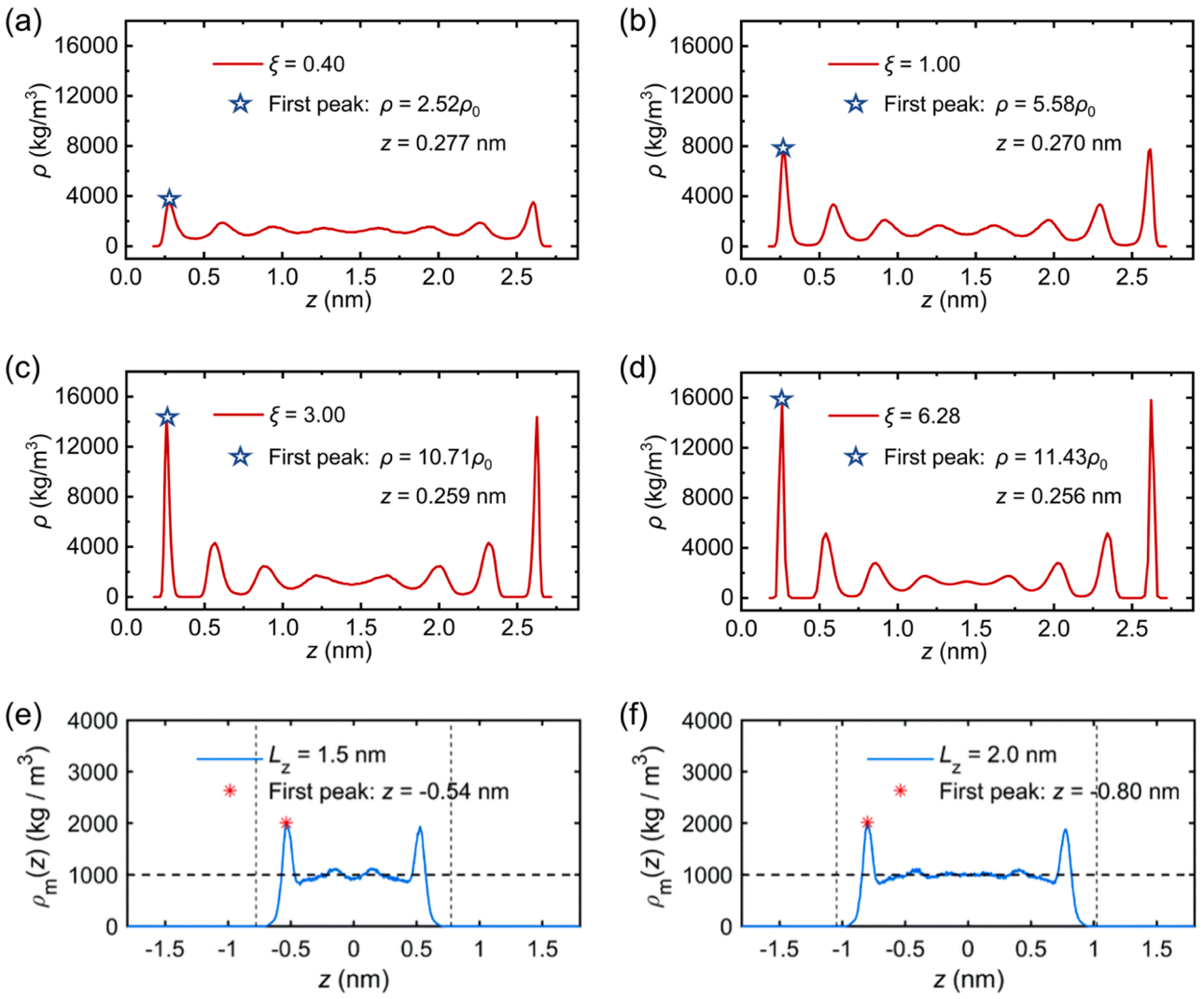

Fig. 3. Density distribution of liquid molecules in the slit with different hydrophilicity coefficients (ξ) and slit heights ($2h$): (a) $\xi = 0.40$, (b) $\xi = 1.00$, (c) $\xi = 3.00$, (d) $\xi = 6.28$, (e) $2h = 3$ nm, (f) $2h = 4$ nm. (e) and (f) are derived from the literature [35]. Z-axis is the slit height direction. The hydrophilicity coefficient ξ denotes the membrane's hydrophilicity level, defined as the ratio of solid-liquid particle potential energy intensity to that of liquid-liquid particle interactions.

Due to the small size effect, nano-confined fluids exhibit anisotropic viscosities. For the current model, when calculating the viscosity of the thermally driven flow in the x-direction, it is imperative to account for the pressure in the z-x plane. Within a given horizontal plane of the flow channel (consistent z-coordinate), the fluid particles are relatively uniformly dispersed, and in accordance with the pressure Eq. (21), the statistical average of the second term on the right side is expected to approach zero. Within the same cross-sectional area of the channel (identical x-coordinate), the temperature remains uniform, thereby rendering the pressure proportional to the molar density. Upon reintegrating this outcome into Eq. (20), considering that the time autocorrelation function of the pressure is magnified by the volume (V), the resultant viscosity is deduced to be proportional to the molar density, as delineated in Eq. (22).

$$\frac{\eta(z)}{\eta^{\mathrm{ave}}} = \frac{\rho(z)}{\rho^{ave}} \tag{22}$$

Where η(z) and ρ(z) represent the local liquid viscosity and density, respectively. Superscript *ave* represents the average value of the physical properties. By substituting this formula into Eq. (19), the thermo-osmotic velocity of liquid layers with different heights can be calculated. The average liquid viscosity in a slit can be calculated based on the following formula:

$$\eta_0 = \frac{b(2\mathrm{h} - \sigma_{S-L})^3 \Delta P}{12Ql} \tag{23}$$

where l, b, and $2h$ are the magnitude of the slit in the x, y, and z directions, respectively, ΔP is the pressure difference between the reservoirs on both sides of the slit, and Q is the flux. The mean value of the liquid viscosity can be calculated by counting the flux of the liquid through the slit under the external pressure.

3.2.4. *Validation of theoretical calculations*

As mentioned above, after eliminating the interference of the boundary on the calculation, it becomes problematic to determine the velocity boundary in the center of the channel. Considering the features of nanoconfined fluid, we performed two simulations with external pressure-driven and temperature-driven fluid flow in the nano-slit, respectively. The former is used to determine the velocity boundary of the channel center. Fig. 5 (a) shows the density and velocity distribution curves of fluid in the flow channel driven by external pressure, while Fig. 5 (b) shows the results of MD simulations and calculations with Eq. (19) for the thermo-osmotic velocity distribution in a temperature-driven flow channel.

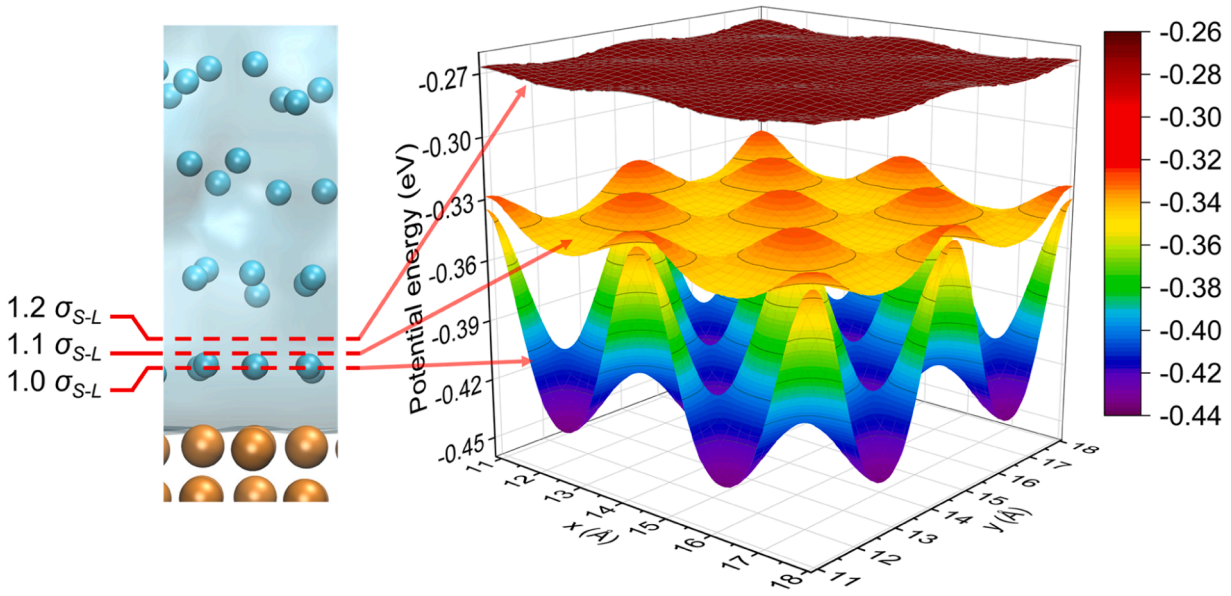

Fig. 4. Potential energy distribution generated by wall particles for liquid particles at different heights

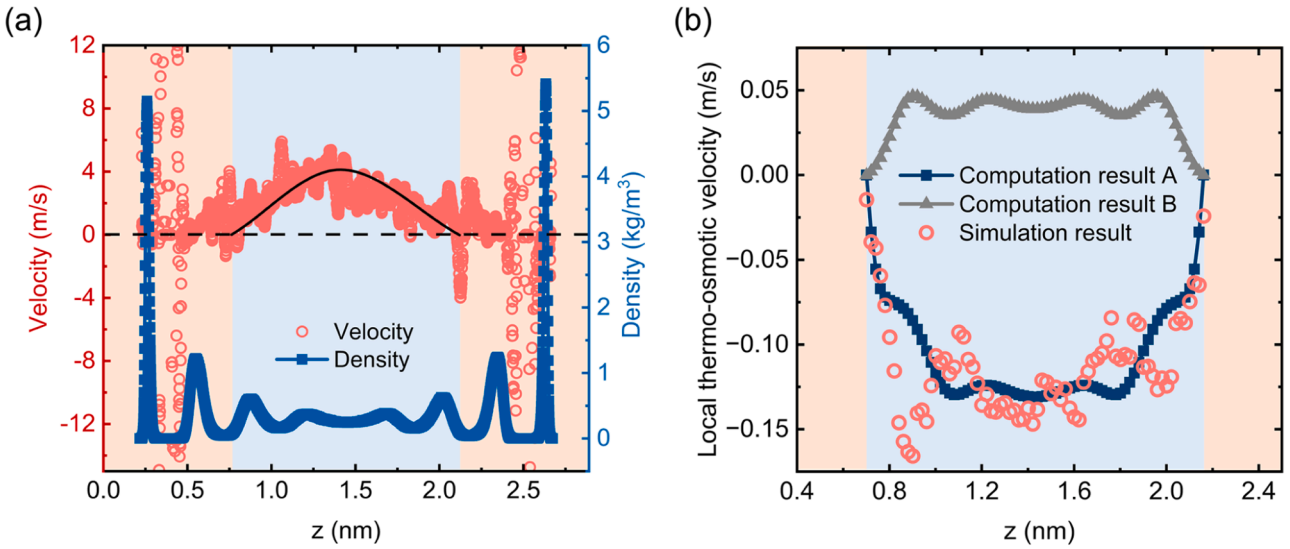

Fig. 5. Velocity distribution curve in the flow channel, the blue region is the region where the continuity assumption is valid, and the rest of the regions are not valid: (a) Density and velocity distributions of the fluid in the flow channel driven by external pressure, where the black solid line is the fitted curve of the fluid velocity; (b) MD simulation results and theoretical calculation results of the fluid velocity distribution driven by temperature, where computation result A takes into account the spatial variation in viscosity, while computation result B does not.

Both simulations were modeled as shown in Fig. 1 (a), with the pressure-driven simulation applying isotropic pressure on the left and right pistons. For the temperature-driven simulation, the cold and hot end temperatures are 86 K and 110 K, respectively, while the slit height was maintained at 2.89 nm. The thermo-osmotic velocity distribution obtained from the simulation is depicted in Fig. 5 (b), alongside the distribution calculated according to Eq. (19). The computation result A takes into account the spatial variation in viscosity, whereas computation result B does not.

In Fig. 5 (a), the region where the fluid continuity assumption holds is identified by the blue background color, where the fluid density is always greater than zero and the fluid particles are all free-flowing. The black curved solid line is the velocity distribution curve fitted to the middle fluid in the MD simulation, and the data show that the velocity at the middle fluid boundary should be zero, so it is appropriate to take zero for the slip length b. After we substitute $b = 0$ into Eq. (19) to obtain the theoretically calculated curve for the thermo-osmotic velocity, it is compared with the MD results. The velocity distribution results of MD are the statistical average obtained from seven independent simulations, which can be used in mitigating the disturbances caused by the irregular motion of molecules.

The data in Fig. 5 illustrate that computation result A, which incorporates the spatial transformation of viscosity, closely matches the MD simulation outcomes. Given the rarity of studies calculating the thermo-osmotic velocity via the formula, this paper conducts a comparison between computation result A, which factors in the spatial variation of viscosity, and computation result B, which does not. It is observed that the thermo-osmotic velocity computed by computation result B diverges from the actual simulation results, exhibiting a significant discrepancy in magnitude and direction. The primary cause of this discrepancy lies in the reduced fluid density at the boundary of the effective flow region, as per Eq. (22), leading to a decrease in fluid

viscosity and an increase in the rate of fluid velocity changes, which is crucial for the generation of thermo-osmotic velocity. The comparison of these three outcomes underscores the necessity of accounting for viscosity changes in the calculation of thermo-osmotic velocity within the effective flow region.

The correlation coefficient between Calculated Result A and the simulated results is $r = 0.63$. The error stems from two main sources: First, the slip length b cannot be accurately determined. Second, the spatial scale of the statistics is relatively small, which means that the statistical results may be skewed by the random thermal motion of molecules. The simulation results of the velocity distribution correlate well with those reported by Fu et al. [32], thereby affirming their reliability. The results elucidate the driving principles of thermo-osmosis and further clarify the interrelation between thermo-osmotic velocity, liquid viscosity, ESE, and temperature gradient.

As illustrated in Fig. 5 (b), the calculated thermo-osmotic velocity distribution appears to be formed by the connection of multiple line segments with discontinuous slopes, this is attributed to the excess specific enthalpy exhibiting sharp fluctuations at different positions. In regions of high density, the ESE of the liquid undergoes significant fluctuations. It can be inferred that the trend of thermo-osmotic velocity within this domain will exhibit a marked change, corresponding to the inflection points delineating regions of thermo-osmotic velocity alteration. If the local thermo-osmotic velocity is multiplied by the molar density and averaged across the channel section, the TOF can be obtained. Integration of the data in Fig. 5 (b) reveals that the difference of the TOF between the theoretical calculations and the MD simulations is about 7.0 %, which confirms the correctness of the theoretical calculations

3.3. Simulation results and mechanism analysis

This part shows the effect of four influencing factors on thermo-osmosis through MD simulation results and makes an analysis of the mechanism. To reduce the measurement error of the TOF, five independent simulations were carried out for each condition of measuring, and the mean and standard deviation of the five simulation results were calculated and shown in Fig. 6. The data exhibited in Fig. 6 demonstrate a significant correlation between the TOF and system temperature, pore size, and the hydrophilicity of the nano-porous membranes. Conversely, the results suggest that the TOF is minimally influenced by the pore geometry of the membrane.

3.3.1. Changes in TOF

Analysis of data from Fig. 6 demonstrates that, under the simulated conditions, an elevated hot end temperature or a wider nanochannel will increase thermo-osmotic flux. The effect of hydrophilicity of the porous membrane on the thermo-osmosis is more complicated. The MD

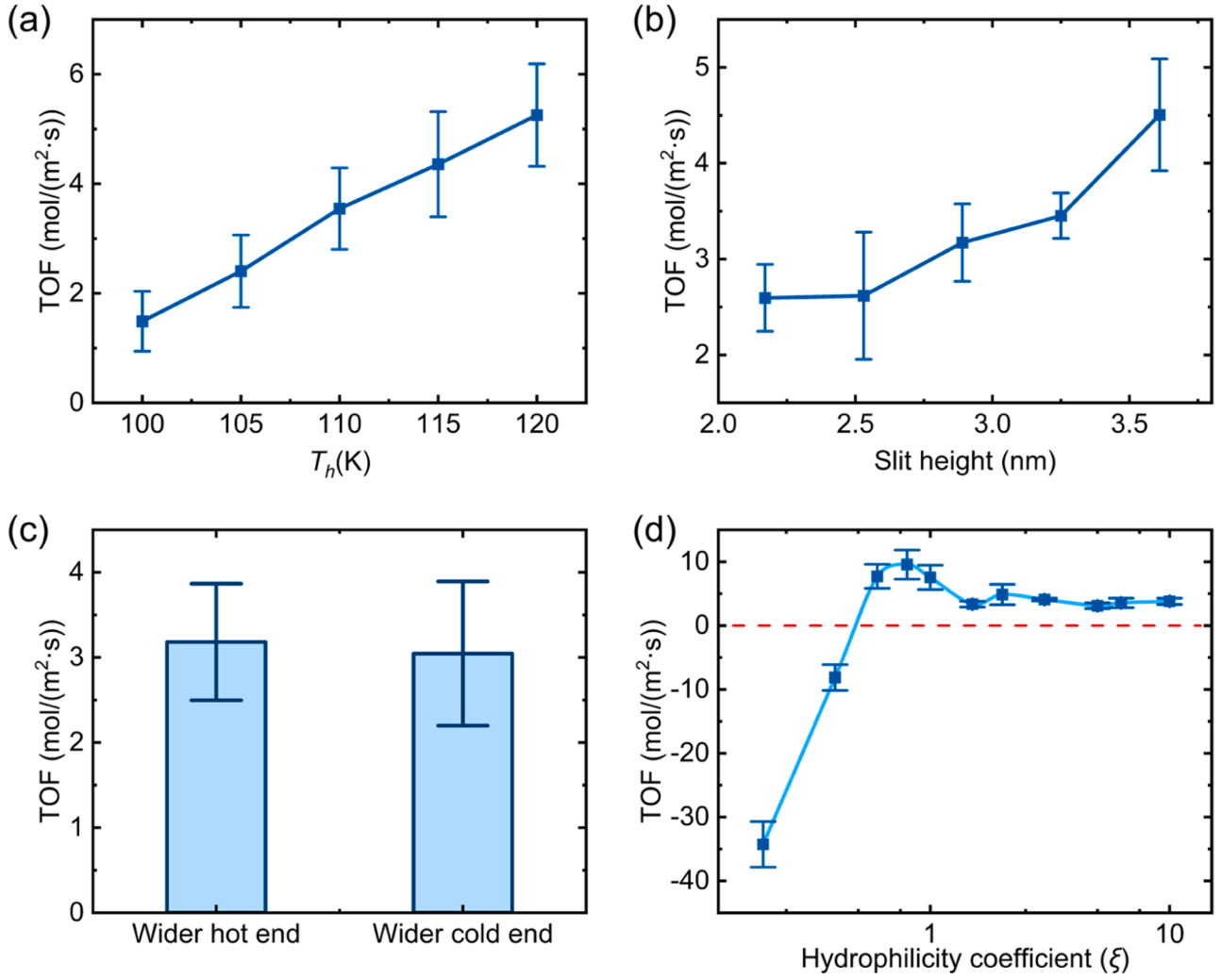

Fig. 6. Variation of thermo-osmotic flux (TOF) with: (a) Hot end temperature (T_h), (b) Slit height, (c) Slit geometry, and (d) Wall hydrophilicity coefficient (ξ), denotes the membrane's hydrophilicity level, defined as the ratio of solid-liquid particle potential energy intensity to that of liquid-liquid particle interactions. Error bar: Standard deviation.

simulation results reveal that for porous membranes with a hydrophilic coefficient ranging from 0.6 to 10.0, the solid-liquid contact angle approaches 0°, aligning with the findings of Fu et al. [32]. Within this range, the direction of thermo-osmosis matches the direction of temperature increase, and the TOF tends to increase as the hydrophilicity coefficient decreases. When the hydrophilicity coefficient is reduced to 0.4, the contact angle of the solid-liquid reaches approximately 43°, resulting in a reversal of the thermo-osmosis flow corresponding to temperature reduction. If the hydrophilicity coefficient is further reduced to 0.2, the TOF will be further enhanced. However, lowering the hydrophilicity coefficient of the porous membrane to 0.1 results in a wall contact angle of 142°, preventing liquid infiltration into the interior of the porous membrane. The model in this case is shown in Fig. A3 in the Appendix.

In the thermo-osmotic simulations conducted by Wang et al. [39], it is observed that when the hydrophilic coefficient approached 0.5, the direction of thermo-osmosis reverses, and the thermo-osmotic flux of the hydrophobic material is notably higher. Our study expands upon the range of influencing factors and delves into the mechanisms underlying the impact of each factor on thermo-osmotic fluxes, considering both resistance and dynamics, as detailed in the subsequent section.

3.3.2. *Changes in viscosity*

To uncover the nanoscale mechanisms governing the influence of the specified factors on thermo-osmosis, an analysis of flow resistance and generalized thermo-osmotic drivers was conducted. To examine the effects of the identified factors on flow resistance, the model utilized for the thermo-osmotic simulations was employed, but the simulation process and control factors are changed. In this segment of the research, liquid flow was initiated by directly applying an external force, in contrast to utilizing a temperature gradient, thus facilitating a comparative analysis of flow resistance changes under a consistent driving force. Flow resistance for each scenario is assessed by comparing the pressure-driven flux (PDF) and the viscosity of the liquid [40]. The temperature difference between the reservoirs at opposing ends is canceled during the simulation, and the temperature of the system was uniform. A pressure of 50 bar in the positive x-axis direction was applied to both pistons as the external thrust to drive the liquid flow. After full relaxation, a 15 ns MD simulation was carried out to measure and record the PDF for each condition, with the mean viscosity of the fluid being computed according to Eq. (23). Fig. 7 presents the compiled data for PDF and mean liquid viscosity under the applied external force conditions.

The data in Fig. 7 indicate that under a constant external driving force, elevating the system temperature, enlarging the slit height, or diminishing the hydrophilicity of the porous membrane contributes to a reduction in liquid viscosity and an enhancement of the PDF; conversely, altering the flow channel's geometry has a negligible impact on the flow

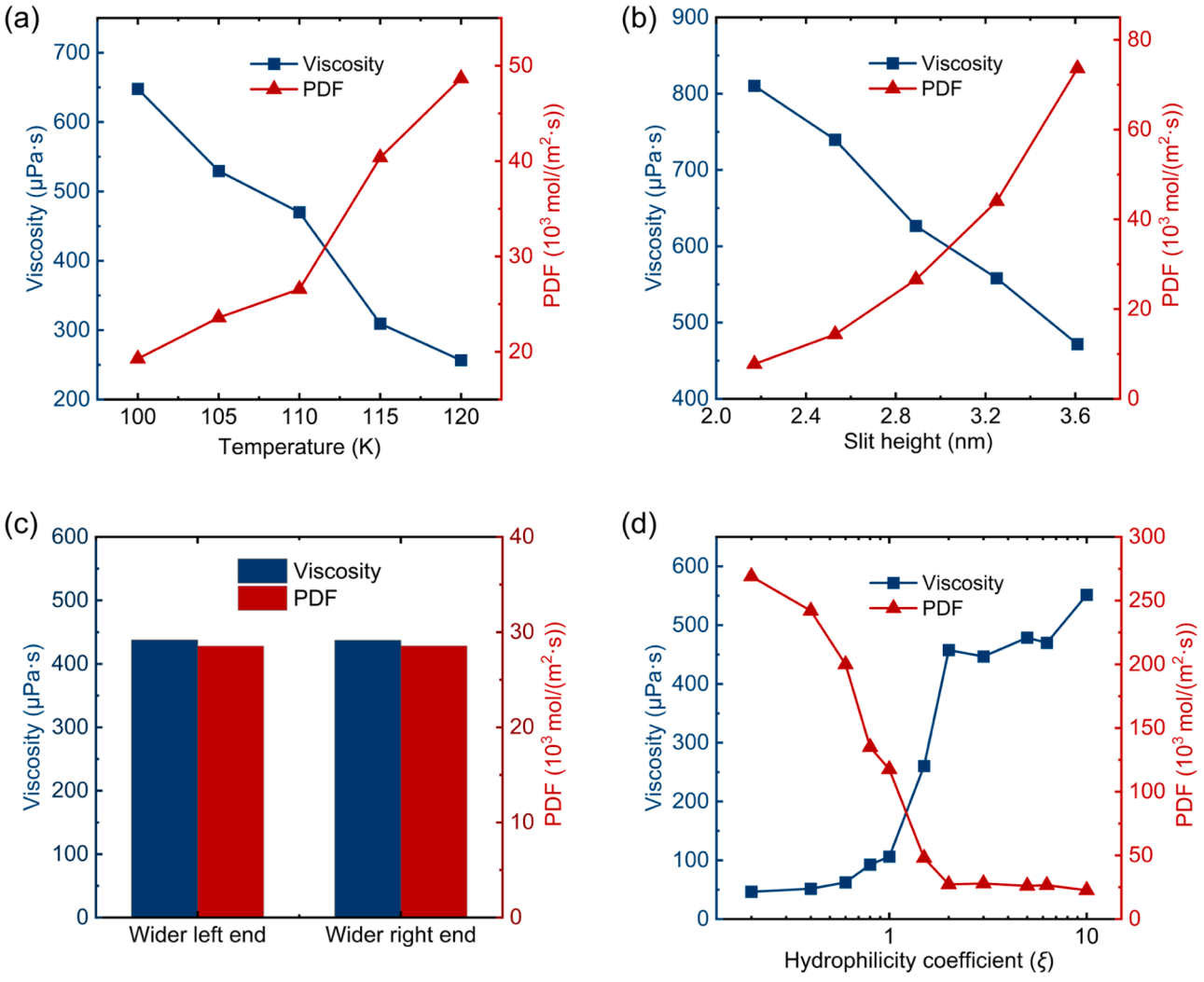

Fig. 7. Variation of viscosity and pressure-driven flux (PDF) with: (a) System temperature, (b) Slit height, (c) Slit geometry, and (d) Wall hydrophilicity coefficient (ξ).

resistance.

System temperature's major impact on liquid flow resistance is due to higher liquid temperature leading to lower viscosity. Consequently, a liquid at a higher temperature is expected to demonstrate a greater flux under the identical external driving force. In the thermo-osmosis simulation, maintaining the cold end's temperature constant while elevating the hot end's temperature leads to an increased overall temperature of the fluid within the flow channel, subsequently diminishing the flow resistance.

Elevating the slit height augments the total number of fluid particles within the flow channel, concurrently diminishing the proportion of fluid particles attracted to the wall particles. It is evident that an increase in the slit height mitigates the resistance of the wall particles to the overall adsorption of fluid particles, consequently alleviating the flow resistance within the channel.

The hydrophilicity coefficient of the porous membrane is pivotal in dictating liquid flow resistance. A diminished hydrophilicity of the membrane leads to a weakened interaction between solid and liquid particles, resulting in reduced wall viscosity resistance. With a consistent driving force, the smaller flow resistance of the liquid in the slit, the larger liquid PDF. Reducing the flow resistance of the thermo-osmosis flow has an obvious promoting effect on the thermo-osmosis. Combined with Figs. 6 and 7, it is evident that the TOF tends to be greater under conditions of reduced flow resistance.

3.3.3. Changes in ESE

To investigate the effects of the aforementioned factors on the generalized driving force of thermo-osmosis, the distribution of the liquid's ESE under various conditions was quantified. Given that the pore geometry exerts minimal influence on both the TOF and the flow resistance, its impact on the ESE is consequently disregarded. The liquid within the slit is categorized into multiple segments along the z-axis, and the intensity and orientation of the generalized driving force for each scenario are assessed and contrasted by determining the ESE of liquid particles within each segment. The distribution curves of ESE of the liquid in the slit along the z-direction under each condition are shown in Fig. 8. Because of the symmetry of its distribution in the z-direction in the slit, only half of the ESE curves in the flow channels are drawn, and the axis of symmetry is denoted by a vertical dotted line.

Fig. 8 (a) and (b) show that changing the system temperature and slit

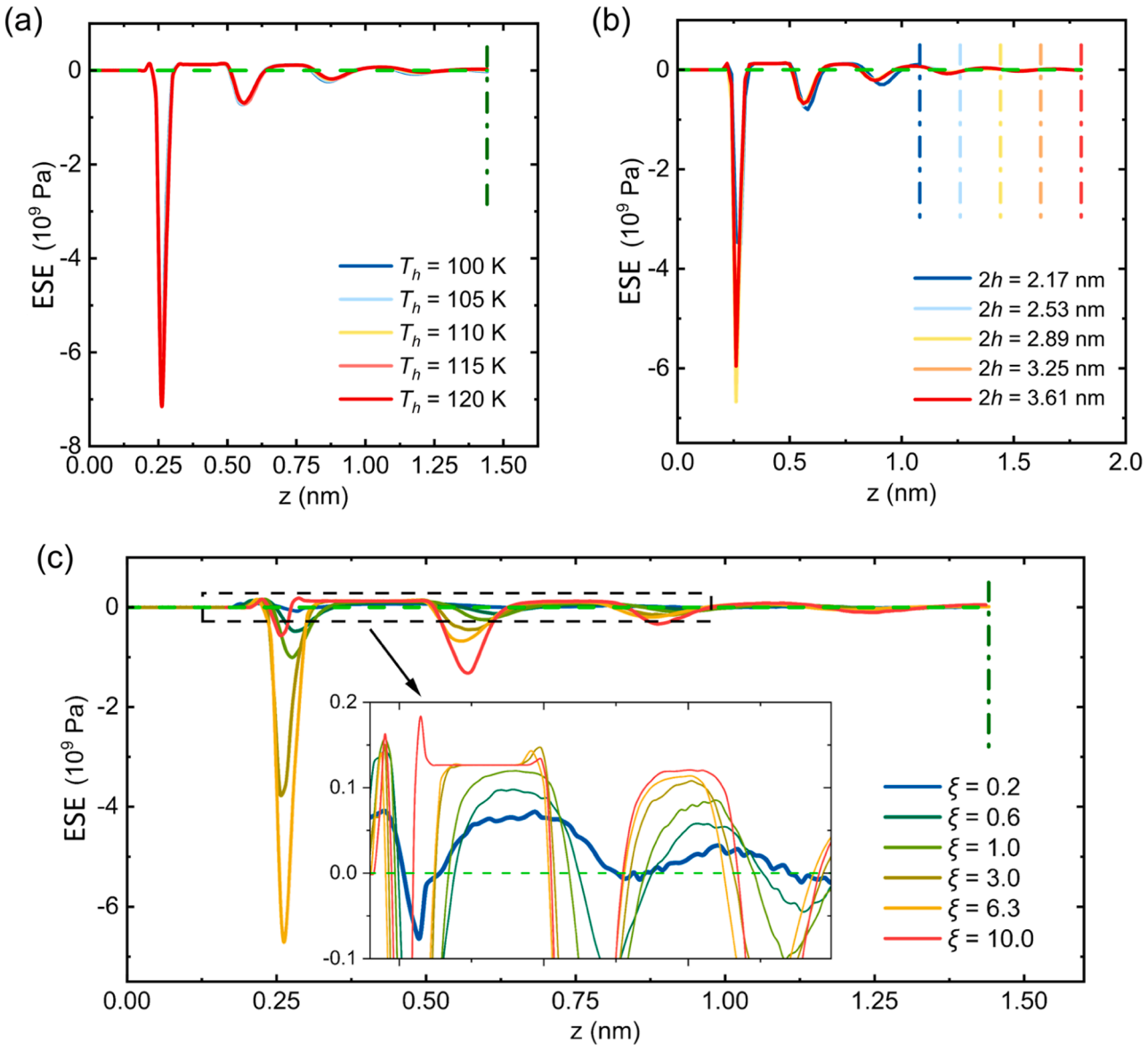

Fig. 8. Distribution curve of excess specific enthalpy (ESE) of liquid in the slit: variation of ESE with: (a) T_h, (b) Slit height ($2h$), and (c) Wall hydrophilicity coefficient (ξ).

height demonstrates little effect on the ESE of the liquid in the slit, as indicated by the near-coincidence of all curves. Only the ESE of the liquid in the wall-attached layer fluctuates to a certain extent. According to the analysis in section 3.2, the liquid particles in this layer show a quasi-crystalline lattice structure under the influence of the wall particles and are unable to flow, thus the ESE of the liquid in this layer can be neglected when calculating the thermo-osmotic velocity. Fig. 8 (c) illustrates that, for walls exhibiting strong hydrophilicity, the overall ESE within the slit registers below zero. The direction of thermo-osmotic flow, as inferred from Eq. (19), is predicted to align with the temperature gradient; that is, the fluid tends to flow towards the hotter end. Combined with the simulation results in Fig. 6 (c), the liquid flows to the hotter side in the highly hydrophilic slit and to the colder side in the weakly hydrophilic slit. A robust congruence between theoretical predictions and simulation results is evident. The data presented in Fig. 7 (a) and (b), along with Fig. 8 (a) and (b), reveal that the TOF enlarges with the increase of the temperature at the hot end, because the increase of the temperature not only reduces the flow resistance in the slit, but also increases the temperature gradient of the liquid in the slit. The main reason for the increase of TOF with the increase of slit height is that the increase of slit height weakens the overall flow resistance of the wall to the liquid. Eq. (19) proficiently explains the observed trends in the variation of thermo-osmotic flow.

Fig. 8 (c) illustrates a marked impact of the hydrophilicity coefficient on nano-porous membranes' ESE within the slit. A higher hydrophilicity coefficient is associated with a reduced ESE, which reflects in the thermo-osmotic velocity formulated in Eq. (19) and encourages the liquid to move towards the hot end. For a porous membrane with a sufficiently small hydrophilicity coefficient, the ESE of the liquid generally exceeds zero. Under these conditions, the thermo-osmotic flow is in the opposite direction of the temperature gradient, with the liquid within the slit flowing to the cooler regions. This is in line with the simulation findings for thermo-osmosis in porous membranes featuring hydrophilicity coefficients of 0.2 and 0.4. The aforementioned simulation outcomes corroborate the calculations of thermo-osmotic velocity, thereby verifying the accuracy of Eq. (19) and establishing the relationship between ESE and thermo-osmotic velocity.

3.3.4. *Changes in the internal energy density and liquid pressure*

To elucidate the cause behind variations in liquid specific enthalpy within porous media exhibiting diverse hydrophilicity coefficients, specific enthalpy is decoupled to the internal energy density (IED, denotes the internal energy of the liquid per unit volume) and liquid pressure. Distribution curves for both IED and pressure of the liquid within the flow channel have been separately quantified and depicted in Fig. 9.

Comparing the simulation results of Chen et al. [24], it can be found that the liquid pressure only fluctuates greatly near the wall, which shows that the results of the present simulation are credible. The curves reveal that with an ascending hydrophilicity coefficient of the porous membrane, there is a downward trend in internal energy density, alongside a continuous rise in liquid pressure, most notably within the particle layers adjoined to the wall. Analyzing the trend of curves in Fig. 9, the pressure of the liquid particles in the wall-attached layer is more sensitive to the change of the hydrophilicity coefficient of the porous membrane compared to the internal energy density, which is the reason that the ESE of the liquid in the wall-attached layer rises instead when the hydrophilicity coefficient of the wall is increased to 10.0.

Through variations in IED and pressure, the underlying cause for alterations in liquid specific enthalpy can be elucidated. Modifications in the hydrophilicity coefficients of the wall material induce changes in the configuration of liquid particle arrangements. Based on the potential function, it is evident that the interaction forces between solid-liquid inter-particles and liquid-liquid inter-particles are subject to alteration. Consequently, the hydrophilicity coefficients of the wall material exert an influence on the liquid-specific enthalpy.

4. Conclusion

In this study, we refined the equation for calculating the thermo-osmotic velocity distribution within a slit to incorporate the spatial variation of fluid viscosity. We also defined the effective thermo-osmotic region to eliminate the effects of near-wall adhesion and density stratification on the calculation of the thermo-osmotic velocity. By synthesizing these two improvements, we achieved a quantitative calculation of the thermo-osmotic velocity distribution. Under the conditions of a temperature difference of 24 K and a slit height of 2.89 nm, the average thermo-osmotic velocities obtained through MD simulation and the improved computational method were -0.113 m/s and -0.105 m/s, respectively. Despite the influence of irregular molecular thermal motion, the correlation coefficient of the thermo-osmotic velocity distribution obtained through calculation and simulation was approximately 0.63. The error in the TOF derived from the integration was only about 7.0 %. Conversely, if the traditional method that neglected viscosity

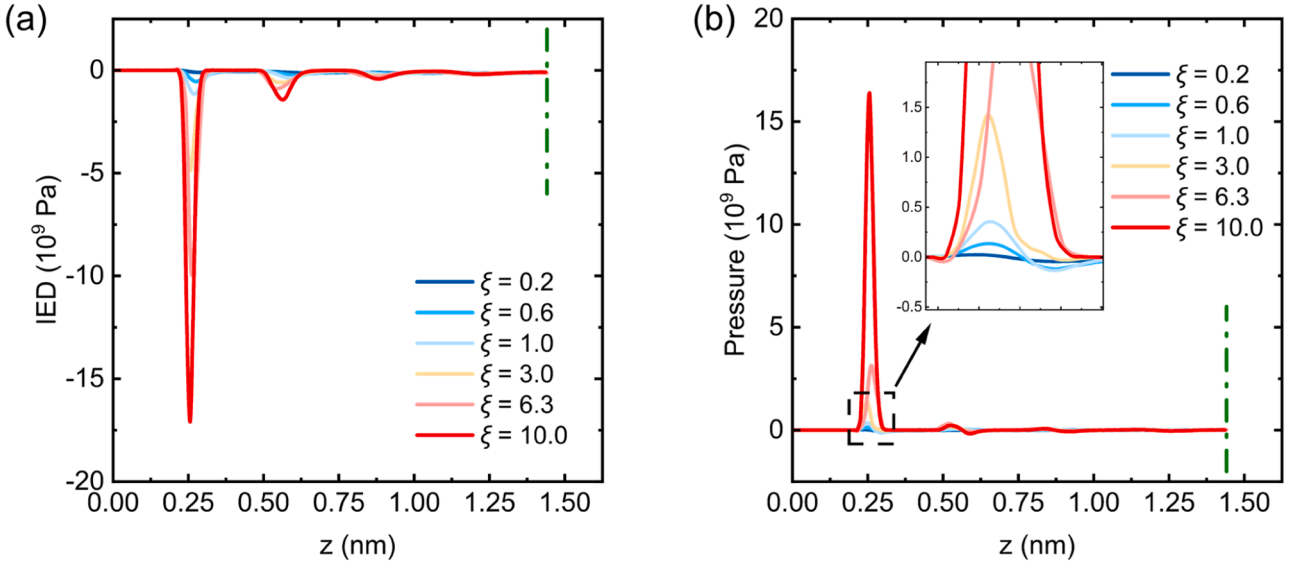

Fig. 9. Distribution curves of liquid: (a) Internal energy density (IED, internal energy per unit volume) and (b) Pressure in the slit.

variations was employed, the calculated average thermo-osmotic velocity within the slit was 0.036 m/s, which significantly differed from the simulation results both in magnitude and direction. This inconsistency highlighted the crucial need for the enhancements implemented in the traditional thermo-osmotic velocity calculation method.

In order to further exploring the control method of thermo-osmosis, the effects of temperature, slit height, slit geometry and the hydrophilicity of membrane material on the thermo-osmosis were systematically examined. Building upon this foundation, an in-depth analysis was conducted to explore the effects of these factors on resistance and driving force, clarifying the underlying mechanisms of their influence. Within the simulation parameters, an elevation in the hot end temperature and an increase in the slit height both result in an augmented thermo-osmotic flux. These two factors primarily affect the flux by altering flow resistance, with the former also impacting the temperature gradient. Notably, the membrane's hydrophilicity exerts a multifaceted effect on thermo-osmosis; not only can it alter the magnitude of the thermo-osmotic flux by 3 to 10 times, but it can also reverse the direction of the thermo-osmotic flow. Furthermore, utilizing our derived Equation (19), these changes can be aptly explained by the variations in liquid viscosity and excess specific enthalpy. Therefore, the theoretical investigation presented in this study is crucial for elucidating the causes of variations in thermo-osmosis and for establishing optimization criteria for thermo-osmosis across various applications.

Consequently, this investigation reveals key aspects of the thermo-osmotic mechanism and offers strategic guidelines for the development of effective regulatory methods, thereby facilitating proactive utilization of thermo-osmosis in various practical contexts.

CRediT authorship contribution statement

Wenhao Fan: Writing – review & editing, Writing – original draft, Validation, Software, Methodology, Investigation, Formal analysis, Data curation, Conceptualization. **Ji Li:** Writing – review & editing, Supervision, Software, Methodology. **Yubo Tan:** Writing – review & editing, Supervision. **Yifan Zhang:** Writing – review & editing, Supervision. **Wei Liu:** Writing – review & editing, Supervision. **Zhichun Liu:** Writing – review & editing, Supervision, Methodology, Funding acquisition.

Declaration of competing interest

The authors have declared that no conflict of interest exists.

Data availability

Data will be made available on request.

Acknowledgment

This work is supported by the National Natural Science Foundation of China (No. 52076088 and No. 52306085).

Supplementary materials

Supplementary material associated with this article can be found, in the online version, at doi:10.1016/j.ijheatmasstransfer.2024.126153.

Appendix A. Particle distribution of thermo-osmotic fluid

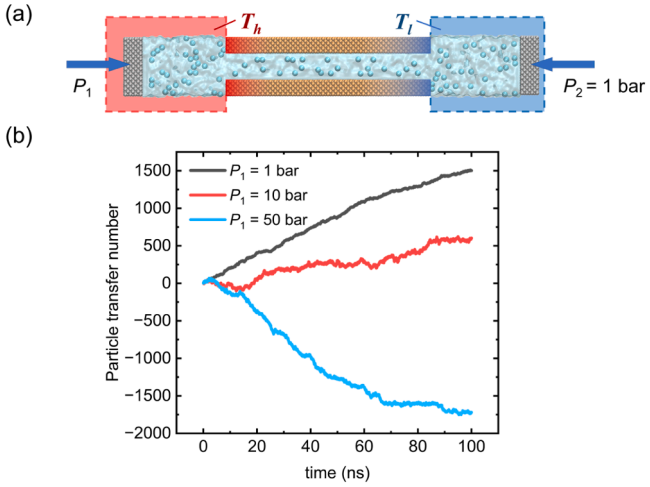

Fig. A1. Thermal osmosis with reverse pressure gradient: (a) Model schematic, apply 1 bar pressure to the cold end piston and change the pressure applied to the hot end piston; (b) Particle transfer number, transfer to the hot end is positive.

It can be found that when 1 bar pressure is applied at the hot end, the pressure at both ends of the slit is balanced, and the fluid particles are driven by thermal osmosis to move toward the hot end. When the pressure at the hot end is increased to 10 bar, the speed of the fluid particles moving towards the hot end decreases significantly, but the particles are still able to transfer against the pressure gradient, indicating that the thermal osmosis has the ability to transfer the thermal energy into the pressure potential energy. If the hot end pressure continues to increase to 50 bar, the fluid particles are mainly driven by pressure and move to the cold end, indicating that the ability of thermal osmosis to drive particles to transfer against the pressure gradient is limited.

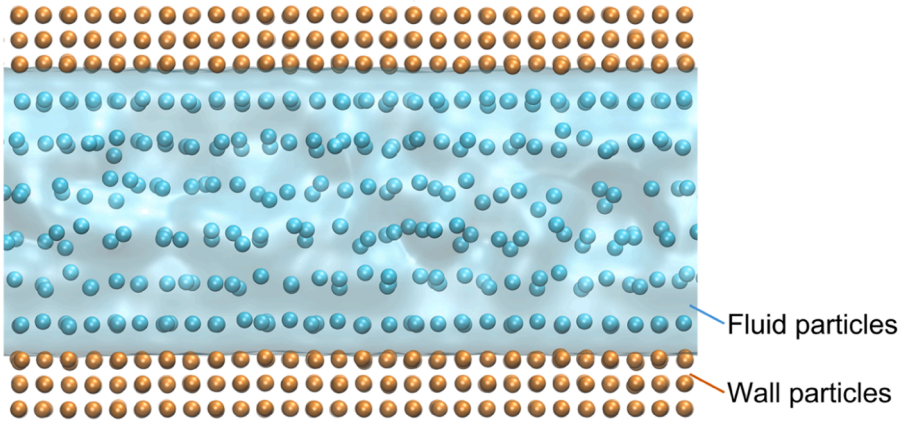

Fig. A2. Particle distribution of thermo-osmotic fluid

Fig. A2 shows the distribution of thermo-osmotic fluid particles in the nano-slit. Obviously, the particles are arranged hierarchically in the slit, and the fluid particles near the wall are neatly aligned with obvious quasi-lattice properties.

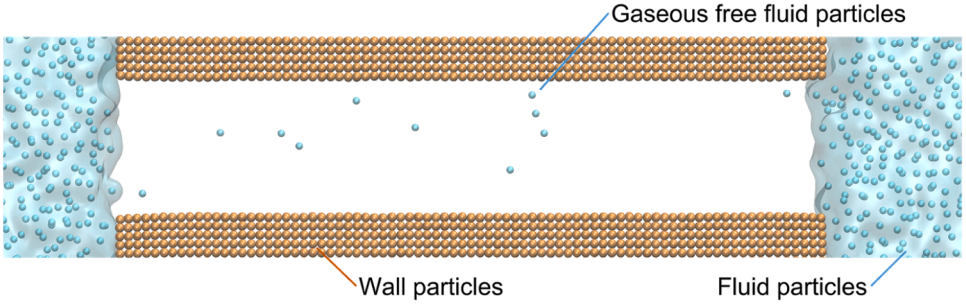

Fig. A3. Modeling of gas-gap thermo-osmosis at a wall hydrophilicity coefficient of 0.1. The hydrophilicity coefficient ξ denotes the membrane's hydrophilicity level, defined as the ratio of solid-liquid particle potential energy intensity to that of liquid-liquid particle interactions.

Fig. A3 shows that when the hydrophobicity of the wall material is enhanced to a certain degree, the liquid will not be able to infiltrate the nano-channels, and only a small amount of gaseous particles are free in the channels. At this time, the liquid-gap thermo-osmosis is transformed into gas-gap thermo-osmosis, and the transfer of particles only depends on the evaporation and condensation rate of the fluid at both ends.

References

[1] V.M. Barragán, S. Kjelstrup, Thermo-osmosis in membrane systems: a review, J. Non-Equilib. Thermodyn. 42 (2017) 217–236, https://doi.org/10.1515/jnet-2016-0088.
[2] M. Ouadfel, M.D.S. Féliciano, C. Herrero, S. Merabia, L. Joly, Complex coupling between surface charge and thermo-osmotic phenomena, PCCP 25 (2023) 24321–24331, https://doi.org/10.1039/D3CP03083K.
[3] H. Xu, X. Zheng, X. Shi, Surface hydrophilicity-mediated migration of nano/microparticles under temperature gradient in a confined space, J. Colloid Interface Sci. 637 (2023) 489–499, https://doi.org/10.1016/j.jcis.2023.01.112.
[4] G. Wang, Y. Ma, W. Chen, Molecular level study of carbon isotope fractionation in Knudsen number flows induced by thermo-osmosis, Int. J. Therm. Sci. 174 (2022) 107441, https://doi.org/10.1016/j.ijthermalsci.2021.107441.
[5] Y. Zhang, J. Li, Z. Zhang, W. Liu, Z. Liu, Enhancing thermo-osmotic low-grade heat recovery by applying a negative pressure to the feed, Glob. Chall. 7 (2023) 2200238, https://doi.org/10.1002/gch2.202200238.
[6] J. Li, Z. Zhang, R. Zhao, B. Zhang, Y. Liang, R. Long, W. Liu, Z. Liu, Stack thermo-osmotic system for low-grade thermal energy conversion, ACS Appl. Mater. Interfaces 13 (2021) 21371–21378, https://doi.org/10.1021/acsami.1c03395.
[7] Q. Deng, K. Meng, W. Chen, G. Yang, N. Zhang, B. Chen, Investigation and evaluation of heat transfer enhancement for PEMFC under high current density based on a multiphase and non-isothermal electrochemical model, Int. J. Heat Mass Transfer 229 (2024) 125738, https://doi.org/10.1016/j.ijheatmasstransfer.2024.125738.
[8] Y. Jin, X. Gao, K. Zhang, Z. Li, A nanopump using carbon nanotube hetero-junction driven by symmetric temperature gradients, Phys. Fluids 33 (2021) 082001, https://doi.org/10.1063/5.0055855.
[9] M. Rastgar, K. Moradi, C. Burroughs, A. Hemmati, E. Hoek, M. Sadrzadeh, Harvesting blue energy based on salinity and temperature gradient: challenges, solutions, and opportunities, Chem. Rev. 123 (2023) 10156–10205, https://doi.org/10.1021/acs.chemrev.3c00168.
[10] S. Kim, M.M. Mench, Investigation of temperature-driven water transport in polymer electrolyte fuel cell: Thermo-osmosis in membranes, J. Membrane Sci. 328 (2009) 113–120, https://doi.org/10.1016/j.memsci.2008.11.043.
[11] X. Zuo, C. Zhu, W. Xian, Q.-W. Meng, Q. Guo, X. Zhu, S. Wang, Y. Wang, S. Ma, Q. Sun, Thermo-osmotic energy conversion enabled by covalent-organic-framework membranes with record output power density, Angew. Chem. Int. Edit. 61 (2022) e202116910, https://doi.org/10.1002/anie.202116910.
[12] W. Xian, X. Zuo, C. Zhu, Q. Guo, Q.-W. Meng, X. Zhu, S. Wang, S. Ma, Q. Sun, Anomalous thermo-osmotic conversion performance of ionic covalent-organic-framework membranes in response to charge variations, Nat. Commun. 13 (2022) 3386, https://doi.org/10.1038/s41467-022-31183-w.
[13] Z. Yuan, Y. Yu, L. Wei, C. Wang, X. Zhong, X. Sui, Z. Yu, D.S. Han, H. Shon, Y. Chen, Thermo-osmosis-coupled thermally regenerative electrochemical cycle for efficient lithium extraction, ACS Appl. Mater. Interfaces 13 (2021) 6276–6285, https://doi.org/10.1021/acsami.0c20464.
[14] J. Li, R. Long, B. Zhang, R. Yang, W. Liu, Z. Liu, Nano heat pump based on reverse thermo-osmosis effect, J. Phys. Chem. Lett. 11 (2020) 9856–9861, https://doi.org/10.1021/acs.jpclett.0c02475.
[15] V.-P. Mai, W.-H. Huang, R.-J. Yang, Charge regulation and pH effects on thermo-osmotic conversion, Nanomater.-Basel 12 (2022) 2774, https://doi.org/10.3390/nano12162774.
[16] H. Shen, Y. Huang, H. Kang, J. Shen, J. Yu, J. Zhang, Z. Li, Effect of the cooling water flow direction on the performance of PEMFCs, Int. J. Heat. Mass Transf. 189 (2022) 122303, https://doi.org/10.1016/j.ijheatmasstransfer.2021.122303.
[17] Y. Li, G. Chang, W. Zhao, Y. Xu, R. Fan, Effects of surfactant CTAB on performance of flat-plate CLPHP based on PEMFC cooling, Int. J. Heat. Mass Transf. 196 (2022) 123226, https://doi.org/10.1016/j.ijheatmasstransfer.2022.123226.
[18] M. Ozmaian, R. Naghdabadi, Modeling and simulation of the water gradient within a Nafion membrane, Phys. Chem. Chem. Phys. 16 (2014) 3173, https://doi.org/10.1039/c3cp54015d.
[19] A. Aman, I.A.A. Khan, U.S. Meda, Water management in PEM Fuel cells, ECS. Trans. 107 (2022) 19403–19413, https://doi.org/10.1149/10701.19403ecst.

[20] X. Wang, L. Jia, C. Dang, H. Li, Wetting behavior of low surface tension liquids on surface with re-entrant topological features, Int. J. Heat. Mass Transf. 229 (2024) 125699, https://doi.org/10.1016/j.ijheatmasstransfer.2024.125699.
[21] S. Ghasemi, M. Khoshvaght-Aliabadi, M.J. Asadollahzadeh, N. Salehi, Improving heat transfer in indirect liquid-based battery thermal management systems through turbulator-equipped conical flow paths, Int. J. Heat. Mass Transf. 229 (2024) 125701, https://doi.org/10.1016/j.ijheatmasstransfer.2024.125701.
[22] R. Ganti, Y. Liu, D. Frenkel, Molecular Simulation of thermo-osmotic slip, Phys. Rev. Lett. 119 (2017) 038002, https://doi.org/10.1103/PhysRevLett.119.038002.
[23] C. Herrero, M. Féliciano, S. Merabia, L. Joly, Fast and versatile thermo-osmotic flows with a pinch of salt, Nanoscale 14 (2022) 626, https://doi.org/10.1039/D1NR06998E.
[24] W.Q. Chen, A.P. Jivkov, M. Sedighi, Thermo-osmosis in charged nanochannels: effects of surface charge and ionic strength, ACS Appl. Mater. Interfaces 15 (2023) 34159–34171, https://doi.org/10.1021/acsami.3c02559.
[25] B.V. Derjaguin, N.V. Churaev, V.M. Muller, Surface Forces, Springer US, Boston, MA, 1987. https://doi.org/10.1007/978-1-4757-6639-4.
[26] E. Brunet, A. Ajdari, Generalized Onsager relations for electrokinetic effects in anisotropic and heterogeneous geometries, Phys. Rev. e 69 (2004) 016306, https://doi.org/10.1103/PhysRevE.69.016306.
[27] D. Reith, F. Müller-Plathe, On the nature of thermal diffusion in binary Lennard-Jones liquids, J. Chem. Phys. 112 (2000) 2436–2443, https://doi.org/10.1063/1.480809.
[28] P. Anzini, G.M. Colombo, Z. Filiberti, A. Parola, Thermal forces from a microscopic perspective, Phys. Rev. Lett. 123 (2019) 028002, https://doi.org/10.1103/PhysRevLett.123.028002.
[29] J. Li, Z. Zhang, Y. Zhang, R. Zhao, H. Cui, T. Zhai, W. Liu, Z. Liu, High heat flux dissipation of membrane-venting heat sink with thin film boiling, Int. J. Heat. Mass Transf. 221 (2024) 125078, https://doi.org/10.1016/j.ijheatmasstransfer.2023.125078.
[30] R. Singh, A.S. Oberoi, T. Singh, Factors influencing the performance of PEM fuel cells: a review on performance parameters, water management, and cooling techniques, Int. J. Energy Res. 46 (2022) 3810–3842, https://doi.org/10.1002/er.7437.
[31] B. Hafskjold, D. Bedeaux, S. Kjelstrup, Ø. Wilhelmsen, Soret separation and thermo-osmosis in porous media, Eur. Phys. J. E 45 (2022) 41, https://doi.org/10.1140/epje/s10189-022-00194-2.
[32] L. Fu, S. Merabia, L. Joly, What Controls Thermo-osmosis? Molecular Simulations Show the Critical Role of Interfacial Hydrodynamics, Phys. Rev. Lett. 119 (2017) 214501, https://doi.org/10.1103/PhysRevLett.119.214501.
[33] C. Herrero, A. Allemand, S. Merabia, A.L. Biance, L. Joly, Chapter: Energy conversion at water-solid interfaces using electrokinetic effects, (2022). https://arxiv.org/abs/2204.13522 (accessed May 7, 2024).
[34] K. Wu, Z. Chen, J. Li, X. Li, J. Xu, X. Dong, Wettability effect on nanoconfined water flow, PNAS 114 (2017) 3358–3363, https://doi.org/10.1073/pnas.1612608114.
[35] W.Q. Chen, M. Sedighi, A.P. Jivkov, Thermo-osmosis in hydrophilic nanochannels: mechanism and size effect, Nanoscale 13 (2021) 1696–1716, https://doi.org/10.1039/D0NR06687G.
[36] M. Qanbarian, A. Qasemian, B. Arab, S. Ebrahiminejad, Explosive boiling of argon on a copper surface coated with graphene/CNT/Cu nanowire; a molecular dynamics study, Int. Commun. Heat Mass Transfer 135 (2022) 106134, https://doi.org/10.1016/j.icheatmasstransfer.2022.106134.
[37] X. Huang, J. Wu, Y. Zhu, Y. Zhang, X. Feng, X. Lu, Flow-resistance analysis of nano-confined fluids inspired from liquid nano-lubrication: A review, Chin. J. Chem. Eng. 25 (2017) 1552–1562, https://doi.org/10.1016/j.cjche.2017.05.005.
[38] C. Sun, R. Zhou, Z. Zhao, B. Bai, Nanoconfined fluids: what can we expect from them? J. Phys. Chem. Lett. 11 (2020) 4678–4692, https://doi.org/10.1021/acs.jpclett.0c00591.
[39] X. Wang, M. Liu, D. Jing, A. Mohamad, O. Prezhdo, Net unidirectional fluid transport in locally heated Nanochannel by thermo-osmosis, Nano Lett. 20 (2020) 8965–8971, https://doi.org/10.1021/acs.nanolett.0c04331.
[40] M. Neek-Amal, F.M. Peeters, I.V. Grigorieva, A.K. Geim, Commensurability effects in viscosity of nanoconfined water, ACS. Nano 10 (2016) 3685–3692, https://doi.org/10.1021/acsnano.6b00187.